communications earth & environment

Article

A Nature Portfolio journal

https://doi.org/10.1038/s43247-026-03572-2

Anatexis of meta-marls generates (silico-) carbonatites in orogenic settings

Chiara Groppo [1] ✉, Fabrizio Tursi [1], Maria Luce Frezzotti [2] ✉, Andrea Maroni [1], Sara Nerone [1] & Franco Rolfo [1]

The genesis of anatectic carbonatites – i.e., rocks crystallized from carbonate melts generated by partial melting of metasediments – remains unclear, though essential to elucidate their occurrence. Reports of anatectic carbonatites are increasing, but their origin from marly metasediments has never been proved. Here we present mesostructural, microstructural and geochemical evidence documenting the origin of anatectic carbonatites through in situ incongruent melting of meta-marls in an orogenic setting. The presence of silicate vs calc-silicate assemblages (K-feldspar vs calcite ± scapolite) interstitially crystallized in distinct domains of the migmatitic meta-marl leucosome indicates late-stage immiscibility between silicate and (silico-)carbonate liquids, preceded by fractional crystallization. The carbonate/silicate melt partition coefficients estimated for major elements are consistent with those experimentally determined for water-bearing silica-rich potassic systems. Our results introduce a new perspective on carbonatite genesis by proposing a viable process for generating carbonate melts in the orogenic crust, challenging the prevailing view that most carbonatites are mantle-derived.

Anatectic processes are mainly studied in metamorphosed pelitic, felsic and mafic lithologies of the continental and oceanic crust because petrological investigation of the natural record of these lithologies is supported by experimental studies and predictions from thermodynamic modelling[1–8]. However, anatectic processes can also occur in carbonate-bearing rocks, which have been rarely investigated, although carbonate-bearing sediments represent relevant components of the continental crust involved in orogenic processes[9,10]. Experimental studies at upper crustal conditions on simplified synthetic systems have highlighted the key role of H_2O, silica and alkalis in lowering the *solidus* of the carbonatic system below 650 °C[11–19]. These conditions are commonly experienced in contact and regional metamorphic settings, suggesting that melting of carbonate-bearing rocks could be more common than currently supposed[17,20]. Different end-member processes are invoked to explain melting of these lithologies as either (i) induced by the intrusion of felsic or mafic magmas[20–24], (ii) related to high-temperature regional metamorphism, or (iii) a combination of these two processes in an evolving orogenic system[25–35]. However, a definitive explanation for the genesis of crustal carbonate melts is still lacking[36,37]. In the absence of experimental data on complex chemical systems and of appropriate solution models for carbonate melts, the investigation of the natural record remains, so far, the only source of information for understanding the response of carbonate-bearing sediments when metamorphosed at high-temperature conditions, typically *supra-solidus* in pelite to felsic systems.

In the last few years, several field occurrences of carbonatite-like rocks in orogenic settings have been reported, interpreted as derived from partial melting of carbonate-bearing sedimentary protoliths (i.e., para-carbonatites[37], or anatectic carbonatites[36]) in relation to mesoscopic structures commonly observed in high-grade metamorphic terranes[38,39]. These lithologies occur as small (cm-sized) veinlets and pods[23,31], metre- to tens of metres wide dykes and/or pegmatites[25,26,29,30,33,34], as well as larger scale (tens of km^2) bodies[32], locally including crustal xenoliths[32,34,35,40]. However, microstructural evidence of the former presence of a carbonate melt is often elusive, especially in slowly cooled migmatites, because they are prone to rapid recrystallization[23,31]. Because clear microstructural evidence of carbonate melts is rare, fewer than twenty case studies have documented anatectic processes in crustal-derived carbonate-bearing rocks[37].

Here we present mesostructural, microstructural and geochemical evidence documenting in situ partial melting of calc-silicate rocks derived from marly sediments metamorphosed at ca. 750–800 °C, and 0.7–0.8 GPa during the Himalayan orogeny[41]. Petrographic observations show compelling evidence of immiscibility between silicate and (silico-)carbonate liquids, indicating that liquid unmixing affects silicate–carbonate sedimentary protoliths at least during the final stages of their anatectic evolution. This interpretation is supported by carbonate/silicate melt partition coefficients for major elements, which are consistent with experimentally determined values for H_2O-bearing silica-rich potassic systems[42]. Our

[1]Department of Earth Sciences, University of Torino, Torino, Italy. [2]Department of Earth and Environmental Sciences, University of Milano Bicocca, Milano, Italy. ✉e-mail: chiara.groppo@unito.it; maria.frezzotti@unimib.it

results have clear implications for understanding the genesis of crustal-derived orogenic carbonatites and demonstrate that anatexis of calc-silicate rocks followed by fractional crystallization and late-stage liquid immiscibility is a viable mechanism to generate carbonate melts in the continental crust. Although it does not question that most carbonatites originate from the mantle, this model challenges the prevailing idea that anatectic melting of crustal rocks cannot produce true carbonatites[43]. It potentially offers an explanation for the origin of carbonatites that lack a clear mantle signature and are found in collisional settings.

Results

Mesostructural features

The studied meta-sedimentary succession is hundreds of metres thick, and consists of calc-silicate gneisses interbedded with dm- to m-thick layers of fine-grained biotitic gneisses (Supplementary Fig. S1d). At the top of the succession, the calc-silicate rocks are overlaid by biotite + garnet-bearing anatectic orthogneisses, which locally host tens of metres thick bodies of garnet + tourmaline-bearing granites characterized by centimetric radial aggregates of sillimanite (Supplementary Fig. S1e). At the outcrop scale, the calc-silicate gneisses show migmatitic texture, mainly stromatitic[38], characterized by the widespread occurrence of leucosome veins and pods hosting large clinopyroxene, garnet and titanite porphyroblasts (Fig. 1), and by an alternation of green and white mm- to cm-thick leucosome and melanosome layers. Leucosome veins and pods range in thickness from about 10 to 50 cm and are either concordant or discordant to the main foliation. The discordant leucosomes are generally coarse-grained, locally pegmatitic, and show sharp and irregular boundaries with the main migmatitic foliation, and host spotted greenish domains dominated by dark-green clinopyroxene and dark-red garnet porphyroblasts (Fig. 1 and Supplementary Fig. S2). Clinopyroxene is often poikiloblastic, ranging in size from 1 to 5-6 cm (Fig. 1 and Supplementary Fig. S2). Garnet is less abundant and has variable size, from 0.5 to 2 cm; it is locally poikiloblastic and is often replaced by a dark-green kelyphitic corona (Fig. 1 and Supplementary Fig. S2). The leucosome assemblage is more challenging to identify, except for mm-sized sulphur grains, which are locally surrounded by an oxidation halo.

Microstructures and mineral chemistry

The studied samples 19a-50_1, 19a-50_2 and 19a-50_3 were collected from the same leucosome pod (Fig. 1). At the microscale, leucosome veins and pods are dominated by K-feldspar, clinopyroxene, scapolite, garnet, calcite, plagioclase and titanite, with minor amphibole, quartz, pyrrothite, rare relics of biotite and accessory apatite, allanite and rutile. An overview of the samples at the thin section scale is shown in Figs. 2, 3a, b and Supplementary Figs. S3, S4, while representative microstructures are illustrated in Figs. 2, 3 and Supplementary Figs. S5–S9; mineral chemical results are summarized in Supplementary Data S1 and Supplementary Figs. S10, S11. Most minerals occur in different generations (discriminated below in assemblages 0 to 4; Fig. 4), which are clearly recognisable according to their grain size, microstructural relationships and composition (mineral abbreviations are after Ref. 44).

The peritectic minerals record. Coarse-grained clinopyroxene (Cpx1), garnet (Grt1), K-feldspar (Kfs1) and titanite (Ttn1) are interpreted as peritectic phases, i.e., the solid products of a melt-producing reaction. The pluri-cm poikiloblastic Cpx1 (*X*Mg = 0.74–0.81) includes coarse-grained euhedral Kfs1 and Ttn1 (Fig. 2a), all minerals showing equilibrium relationships (i.e., straight boundaries and no compositional variations along the inclusion-host contact; Supplementary Fig. S5c). Plagioclase and quartz are also included in Cpx1 but show disequilibrium microstructures. Plagioclase (Pl0: *X*An = 0.35–0.41) has a rounded shape, indicating partial resorption, and quartz (Qz0) is corroded and surrounded by discontinuous films of K-feldspar pseudomorphs after melt (Fig. 2a, sample 19a-50_3). Micro- to meso-perthitic crystals of Kfs1 (*X*Ab = 0.11–0.17) (Supplementary Fig. S5a, b) are either included in Cpx1 or occur as coarse-grained (up to several millimetres in size) crystals in the matrix, generally concentrated in the proximity of Cpx1 (Fig. 3e). Either when included in Cpx1 or in the matrix, Kfs1 hosts fine-grained rounded Qz0, Pl0 and biotite (Bt0) (Supplementary Fig. S5c), which likely represent reactants of the melt-producing reaction. Grt1 ($Alm_{44}Grs_{40}Prp_{13}Sps_2Adr_1$) is pervasively replaced by composite kelyphitic/symplectitic microstructures, which are described below. The size and the shape of these symplectitic domains suggest that Grt1 originally formed pluri-mm-sized porphyroblasts (Fig. 2a), although only small relics are now preserved. As well as Kfs1, the Grt1 is mainly concentrated around the large Cpx1 poikiloblasts (Fig. 2a). Small, rounded calcite inclusions (Cal0) are observed within Grt1 relics, indicating it was a reactant. Ttn1 forms euhedral to sub-euhedral crystals up to several mm in size, and it includes fine-grained Qz0, Cal0 and Pl0 (Supplementary Fig. S5d). Ttn1 is rich in fluorine (F = 0.20–0.28 a.p.f.u.) and has Al = 0.21–0.27 a.p.f.u., inversely correlated with its Ti content. Accordingly, Qz0 + Pl0+Cal0 + Bt0, included in the coarse-grained Cpx1, Grt1, Kfs1, and Ttn1 poikiloblasts, constitute the reactant mineral assemblage that formed the peritectic assemblage coexisting with melt (Fig. 4).

Disequilibrium microstructures between peritectic minerals and the matrix. Cpx1 and Grt1 (i.e., the femic peritectic minerals) show disequilibrium microstructural features with the surrounding matrix. Cpx1 is replaced at the rim and along fractures by a spongy clinopyroxene (Cpx2a: *X*Mg = 0.56–0.74) (Supplementary Fig. S6a). Cpx2a is in optical continuity with Cpx1 and is crowded with fine-grained polyphase inclusions of plagioclase (Pl2a: *X*An = 0.43–0.58), amphibole (Amp2a: pargasite) and calcite (i.e., assemblage 2a; Fig. 4, Supplementary Fig. S6a), forming a network of interconnected inclusions with irregular and vermicular shapes. Grt1 is almost entirely replaced by a composite symplectitic microstructure, which is both texturally and compositionally zoned. The inner portion of the Grt1 reactive domain consists of a fine- to medium-grained symplectitic aggregate of amphibole (Amp2b: potassic-hastingsite), Ca-rich plagioclase (Pl2b: *X*An = 0.73–0.89) and minor clinopyroxene (Cpx2b: *X*Mg = 0.29–0.40) (Supplementary Fig. S6b–d) (i.e., assemblage 2b; Fig. 4). The grain size of the symplectitic aggregate increases outward with respect to the contact with Grt1. In some Grt1 reactive domains, Pl2b is partially replaced by scapolite (Scp3d: *X*Me = 0.76–0.81) (Supplementary Fig. S7); at the contact with Scp3d, the relic Grt1 is overgrown by a thin rim of garnet (Grt3d: $Alm_{41}Grs_{38}Prp_3Sps_7Adr_{11}$). The outer portion of the Grt1 reactive domain consists of a fine-grained granoblastic aggregate of plagioclase, clinopyroxene, calcite and pyrrothite (Supplementary Fig. S7) (i.e., assemblage 3c: Fig. 4). Pl3c has a strongly variable composition (*X*An = 0.60–0.36), being progressively enriched in Na toward the outer portion of the domain. Cpx3c is patchy zoned, with highly variable *X*Mg (*X*Mg = 0.39–0.64), and is often partially replaced at the rim and along cleavages by a late generation of amphibole (AmpL: magnesio-hornblende to actinolite).

Matrix. The matrix hosting the coarse-grained peritectic phases consists of two distinct domains, which differ in mineral assemblages and overall compositions: a silicate domain (a), and a (silico-)carbonate domain (b) (Fig. 3a, b), hereafter indicated as the carbonate domain for the sake of simplicity. The silicate domain consists of K-feldspar and minor quartz and clinopyroxene (i.e., assemblages 3a/4a; Fig. 4). Two different generations of K-feldspar are clearly recognisable based on their grain size: a medium-grained, micro-perthitic Kfs3a (*X*Ab = 0.09–0.13) (Fig. 3c–e and Supplementary Fig. S5a,b), and a fine-grained homogeneous Kfs4a (*X*Ab = 0.08–0.12) (Fig. 3c–e and Supplementary Fig. S9d). The latter is systematically interstitial between Kfs1 and Kfs3a grains, thus defining a sequential microstructure. Cpx3a/Cpx4a (*X*Mg = 0.54–0.63) are locally replaced at their rim by a late amphibole of actinolite composition. The carbonate domain forms rounded ocelli up to a few cm in diameter and shows sharp contacts, suggesting equilibrium with the surrounding silicate domain (Fig. 3b). These ocelli are either isolated within the silicate

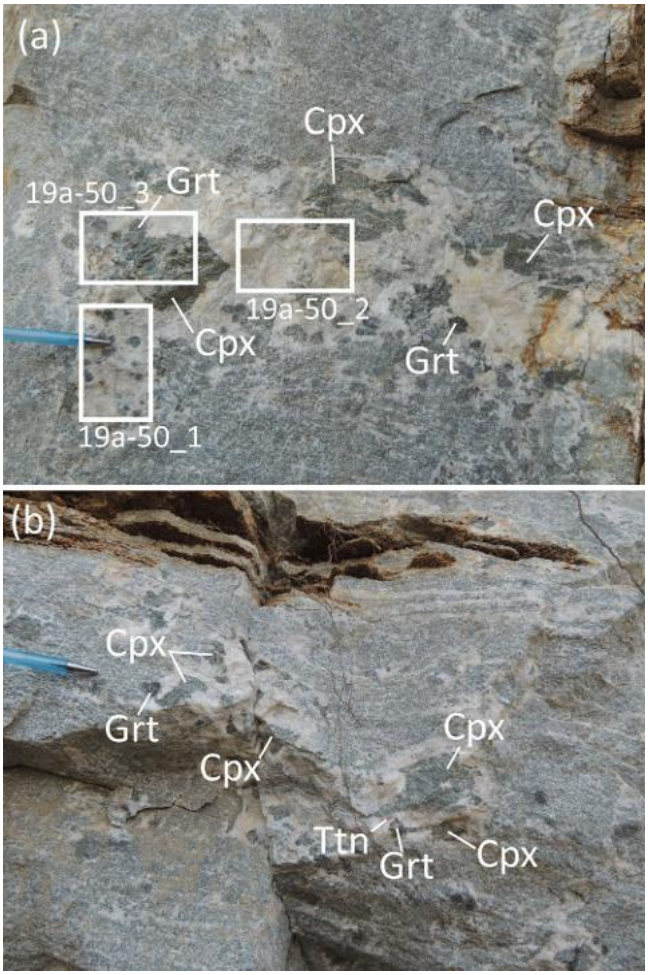

Fig. 1 | Representative images of the studied samples at the outcrop scale. a, **b** The leucosome pods and veins are discordant with respect to the main foliation of the hosting calc-silicate gneisses and have a pegmatitic structure. Pluri-cm dark green clinopyroxene (Cpx) and pluri-mm red garnet (Grt) porphyroblasts, almost completely replaced by dark green kelyphites are set in a whitish matrix, mostly consisting of K-feldspar. The greenish rounded ocelli in the matrix mainly consist of scapolite + clinopyroxene. Blue pen, 13 cm long, for scale. The three thin sections investigated in this study (i.e., 19a-50_1, 19a-50_2 and 19a-50_3) correspond to the domains highlighted by the boxes in (**a**).

matrix domain or adhere to the garnet reactive sites described above. The carbonate domains forming the ocelli consist of fine-grained granoblastic to symplectitic aggregates of scapolite (Scp3b: *X*Me = 0.73–0.76; Cl=0.02–0.09 a.pf.u.), clinopyroxene (Cpx3b: XMg = 0.36–0.48) and minor calcite ± pyrrothite (Supplementary Fig. S8c, d) (i.e., assemblage 3b; Fig. 4).

Thin interstitial polymineralic films consisting either of calcite + clinopyroxene or scapolite + quartz + clinopyroxene (Fig. 2b, c) (i.e., assemblage 4b; Fig. 4), depart from the ocelli and penetrate the silicate domain. In the first type of polymineralic films, calcite shows cuspate terminations with low dihedral angles against the adjacent K-feldspar; scapolite (Scp4b: *X*Me = 0.61–0.70, Cl = 0.13–0.28 a.p.f.u) and quartz in the second type of polymineralic films form fine-grained intergrowths (Fig. 2b). Cpx4b has *X*Mg = 0.52–0.56. Both these types of polymineralic films have the same microstructural features of the so-called pseudomorphs of melt-filled pores described in pelitic migmatites and interpreted as the product of the last melt crystallization (i.e., highly cuspate grains with low dihedral angles[45,46]). The occurrence of fine-grained myrmeckitic microstructures consisting of plagioclase (*X*An = 0.32–0.41) and quartz (Supplementary Fig. S9a–e) at the K-feldspar grain boundaries (i.e., interstitial between adjacent Kfs3a) suggests that K-feldspar interacted with Ca-rich melt/fluid during cooling. Pyrrothite ($Fe_{0.90–0.93}S$) is mainly concentrated within, or in the proximity of, the carbonate domains and systematically occurs in an interstitial position (Supplementary Fig. S9f).

Large polymineralic inclusion within peritectic Cpx1. The peritectic Cpx1 includes a fine-grained polymineralic inclusion a few mm large; around the inclusion, the Cpx1 is replaced by a spongy Cpx2a rim, texturally and chemically similar to that observed at the contact between Cpx1 and the matrix. Two distinct domains are recognisable in the inclusion based on their mineral assemblages; these domains reflect different compositions, which resemble those of the silicate and carbonate domains previously described for the rock matrix (Fig. 2d). The contact between the two domains is sharp. The silicate domain consists of K-feldspar (Kfs3a*: *X*Ab = 0.08–0.11), minor quartz and interstitial amphibole (Amp3a*: hornblende-edenite) (i.e., assemblage 3a*; Fig. 4), this last defining thin interstitial films between K-feldspar crystals. The carbonate domain is composed of plagioclase (Pl3b*: *X*An = 0.52–0.60), amphibole (Amp3b*: potassic-pargasite), calcite, and minor chlorite (i.e., assemblage 3b*; Fig. 4); thin interstitial films of calcite infiltrate from the carbonate domain into the silicate domain.

Bulk compositions of the silicate and carbonate domains

The bulk compositions calculated for the silicate domains in the matrix (i.e., solid assemblages 3a and 4a) have SiO_2 contents of 65.7–67.3 wt.% and $Na_2O + K_2O$ = 14.1–15.0 wt.%, plotting in the trachyte field on the TAS diagram (Supplementary Fig. S13); domain 4a is slightly enriched in SiO_2 and K_2O and depleted in CaO, Na_2O, FeO and MgO compared to domain 3a (Table 1). The silicate domain 3a* in the polymineralic inclusion hosted in Cpx1 is the hydrous equivalent of domain 3a. The carbonate domains in the matrix (i.e., solid assemblages 3b and 4b) have a wider compositional range, with both SiO_2 and $Na_2O + K_2O$ decreasing from domain 3b to 4b (SiO_2 = 43.2–22.5 wt.%; $Na_2O + K_2O$ = 2.7–1.3 wt.%), counterbalanced by an increase of CaO (22.6–38.8 wt.%) and CO_2 (6.8–26.6 wt.%). The carbonate domain 3b* in the polymineralic inclusion hosted in Cpx1 is the hydrous equivalent of domain 3b.

The approximate composition of the whole leucosome pod, obtained by combining the compositions of domains 3a and 3b in a 70:30 ratio as described in the Methods section, is that of a trachyte, with a NBO/T value of 0.23, a #K molar value of 0.77, a K_2O/Na_2O wt.% ratio of 5.00 (Table 1) and a normative composition (vol.%) of Q = 2.9, Pl = 26.2, Or = 56.5, Di = 9.9, Hy = 0.3, Cal = 4.3; therefore the system can be classified as potassic, silica-saturated, according to Ref. 42.

Discussion

Fractional crystallization and liquid immiscibility explain the observed meso- and microstructures

The observed meso- and microstructural features suggest that the studied samples derive from zones of accumulation of anatectic melt produced by in situ partial melting of a marly protolith (Fig. 1, Supplementary Fig. S2). In these melt accumulation zones, porphyroblasts grow to a larger grain size than in melanosome, as typically documented in metapelitic migmatites[47–50]. Accordingly, the melt accumulation zones accreted from in situ leucosomes formed through spatial focussing of the melt-producing reaction around the growing peritectic clinopyroxene[48]. The spatial relationships observed between the leucosomes and clinopyroxene poikiloblasts are analogous to those in garnet-rich leucosomes of metapelitic migmatites[48,49,51]; focussing of the melting reaction around clinopyroxene led to the preferential production of melt and the other peritectic phases (i.e., K-feldspar, garnet and titanite) around the growing clinopyroxene. Mineral assemblages, mineral compositions and microstructural relationships observed in the leucosome's matrix allowed reconstructing a complex anatectic evolution, consisting of a main melt-producing stage (Stage 1) followed by three cooling stages (Stages 2 to 4; Fig. 4). A brief description of each stage is given below and the reconstructed evolution is summarized in Fig. 5.

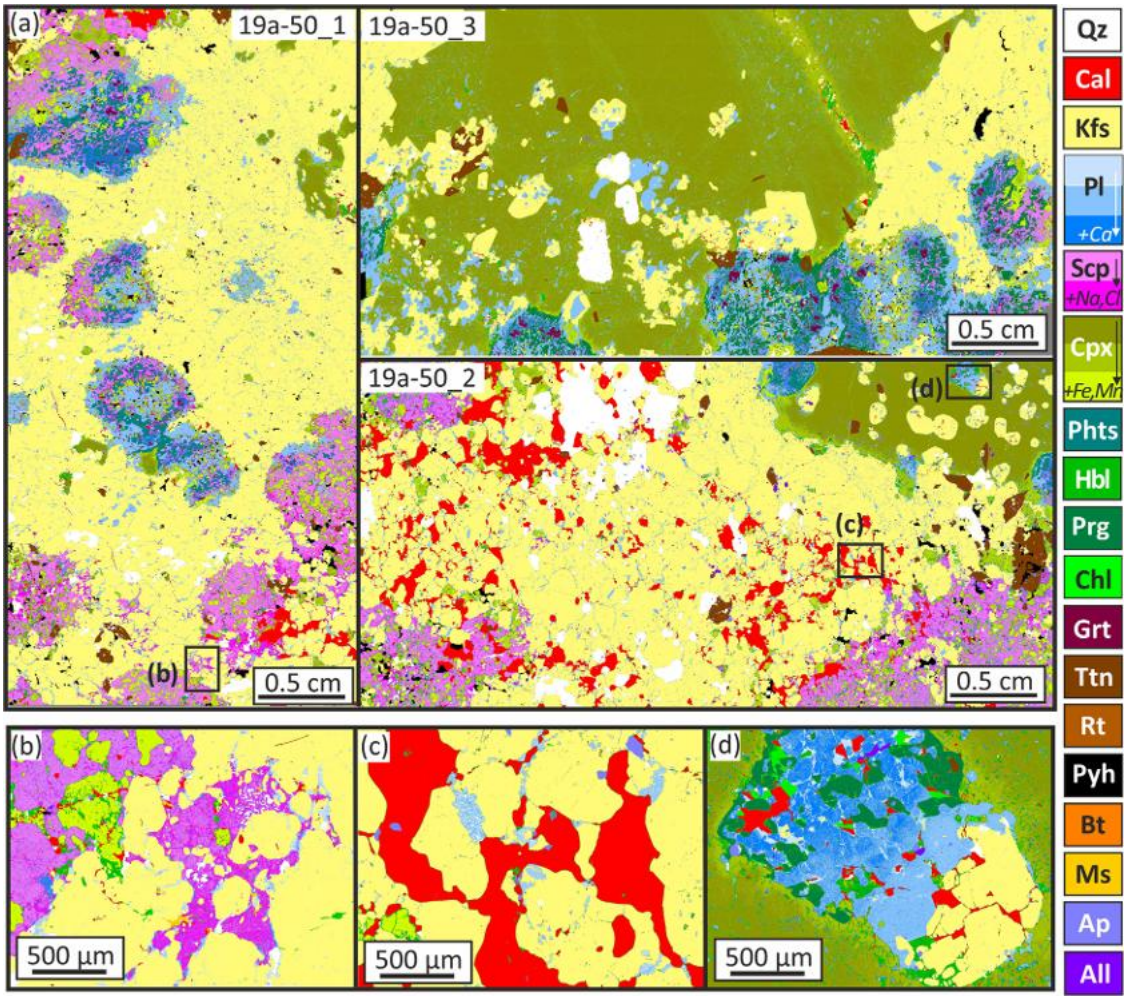

Fig. 2 | Microstructures of the investigated samples at the thin section scale. **a** Processed X-ray maps of the whole thin sections (19a-50_1, 19a-50_2 and 19a-50_3), showing the microstructures of the investigated samples at the thin section scale. **b**–**d** Processed X-ray maps showing representative microstructures of the carbonate domains in the matrix (domains 4b; **b**, **c**) and of the melt pod included within the peritectic clinopyroxene (**d**). In (**d**) note the separation between the Kfs-rich silicate domain and the Pl + Amp + Cal + Chl carbonate domain.

Stage 1: Melt production and growth of peritectic phases. During this stage, an H_2O- and CO_2-rich melt L was produced through the breakdown of calcite (Cal0), biotite (Bt0), quartz (Qz0) and plagioclase (Pl0). Coarse-grained peritectic clinopyroxene (Cpx1), K-feldspar (Kfs1), garnet (Grt1) and titanite (Ttn1) grew in equilibrium with this carbonated silicate melt L. Occasionally, mm-sized pods of melt were entrapped within growing Cpx1; from this stage onward, such inclusions of melt (L*) were isolated from the outside. The bulk composition of the carbonated silicate melt L is approximated by that of the whole leucosome pod (Table 1), except for H_2O, which was likely lost in the subsequent evolution. Experimental studies on CO_2 and H_2O solubility in silicate liquids[52,53] suggest that CO_2 is about one order of magnitude less soluble than H_2O, with CO_2 solubility values generally < 0.5 wt.% for rhyolitic compositions at 0.5 GPa, 800 °C[52,54]. However, CO_2 solubility in silicate melts increases with: (i) increasing pressure and, to a lesser extent, temperature[52]; (ii) decreasing degree of polymerization (i.e., increasing NBO/T values[55]), and (iii) increasing K_2O concentration in the melt, both in term of absolute values (i.e., increasing K_2O wt %[56]) and relative to Na_2O (i.e., increasing #K values[57]). The moderate degree of polymerization (NBO/T = 0.23) and the high K concentration (K_2O = 9.1 wt.%, #K = 0.77) estimated for the melt L, allow us to speculate that the CO_2 solubility in the liquid L was in the range 1–2 wt.%, i.e., higher than that of rhyolitic melts (which have lower NBO/T and #K values), but lower than the very high values of 3–4 wt.% obtained for K_2O-rich nephelinite melts (NBO/T = 1.4; #K up to 1.0) by Ref. 57.

Stage 2: back-reactions between melt and solid phases. During cooling and decompression, the peritectic Grt1 and Cpx1 were no longer in equilibrium with the carbonated silicate melt L and back-reacted with it. A spongy rim of clinopyroxene (Cpx2a) resulted around Cpx1, crowded with amphibole + plagioclase + calcite inclusions (i.e., assemblage 2a). A Cpx2a spongy rim also developed around the mm-sized pod of melt L* entrapped within Cpx1. Grt1 reacted with L at the rim and along fractures, producing back-reaction symplectites consisting of amphibole + plagioclase ± clinopyroxene (i.e., assemblage 2b). A compositional boundary layer (CBL; i.e., interface-melt layer around growing or dissolving crystals with composition different from that of the bulk melt, as defined by Ref. 58, see also Ref. 59) developed around the growing symplectites in the Grt1 reactive domains. The liquid in the CBL concentrated those elements that were not consumed by the minerals growing within the symplectites, thus developing a compositional gradient, particularly evident for Na_2O, which progressively increases outward of the Grt1 reactive domains (Supplementary Fig. S4). Spongy clinopyroxene rims and kelyphitic coronae around garnet are generally described in exhumed mantle xenoliths. Although their formation mechanisms are still controversial[60], the interaction with a melt phase either in the mantle or during transport of the xenoliths to the surface is

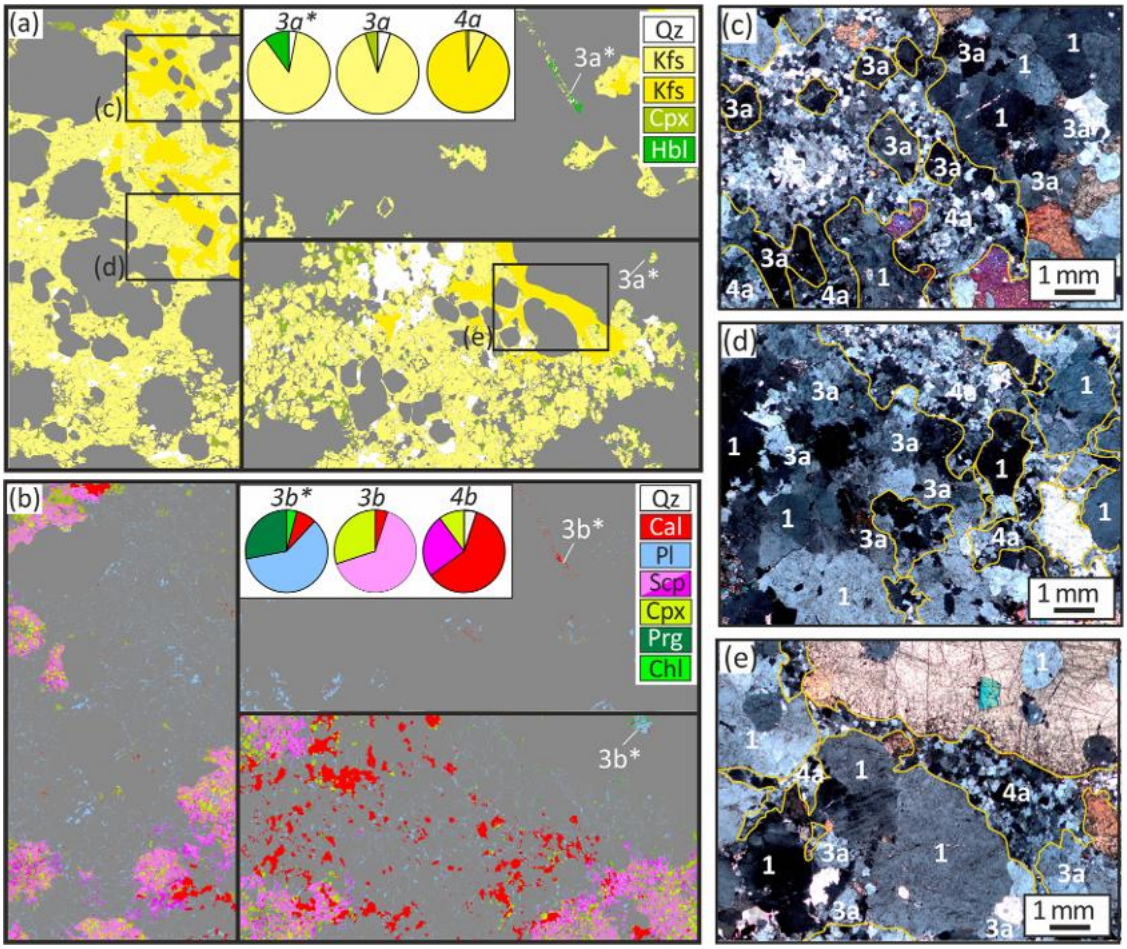

Fig. 3 | Overview of the silicate and carbonate domains. Same processed X-ray maps as in Fig. 2a, highlighting the silicate (**a**) and carbonate (**b**) domains discussed in the text. Other phases not belonging to the silicate and carbonate domains are reported in grey. Modal proportions of mineral phases in the silicate domains 3a*, 3a and 4a and in the carbonate domains 3b*, 3b and 4b are reported in the insets. **c**–**e** Crossed-polarized light images (XPL) highlighting the different silicate domains (i.e., 3a and 4a) within the leucosome matrix. The different K-feldspar generations are recognizable based on their grain size (Kfs1 = coarse-grained; Kfs3a = medium-grained; Kfs4a = fine-grained). Note that domains 4a delimited by the yellow lines, occupy interstitial positions between the previous K-feldspar generations Kfs1 and Kfs3a.

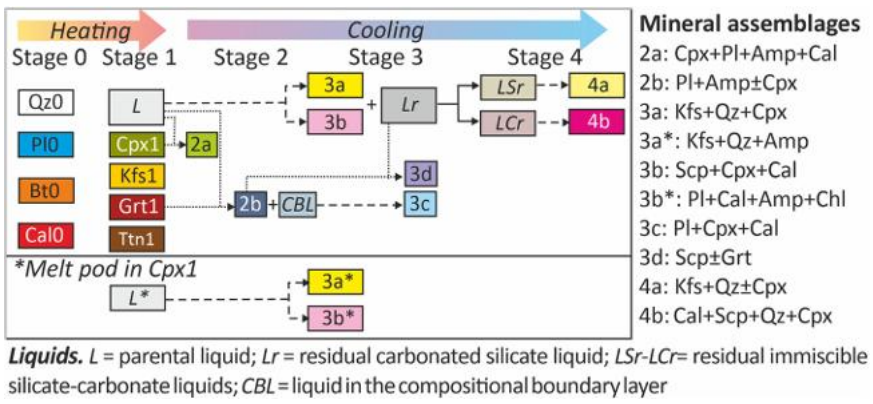

Fig. 4 | Summary of the different assemblages stable during each evolutionary stage. Assemblage 0 represents the *sub-solidus* assemblage stable during stage 0. Note the different style of the arrows: continuous = compositional differentiation of the parental liquid; dotted = back-reactions between melt and solid phases; dashed = crystallization of specific assemblages from the corresponding liquid.

commonly accepted for clinopyroxene[61–63] and has been recently proposed also for garnet[64], further supporting our interpretation.

Stage 3: early crystallization. As the temperature decreased further, the carbonated silicate liquid L began to crystallize. Fractional crystallization induced compositional heterogeneity[65], leading to the crystallization of a silicate assemblage 3a (Kfs + Qz + Cpx) and a calc-silicate assemblage 3b (Scp + Cpx + Cal) in distinct domains of the leucosome matrix, leaving behind a residual carbonated silicate liquid Lr. In the Grt1 reactive sites, assemblage 3c (Pl + Cpx + Cal) crystallized from the CBL liquid, producing the granoblastic aggregates surrounding the Amp + Pl ± Cpx ± Scp symplectites. The composition of Pl3c in these domains reflects the compositional gradient that developed initially within the CBL liquid, i.e., it becomes progressively more sodic toward the external part of the

Table 1 | Compositions of silicate and carbonate domains and of the residual silicate (LSr) and carbonate (LCr) immiscible liquids, and partition coefficients D(LCr/LSr)

Liquid composition					LSr	LCr	L	D(LCr/LSr)
Mineral assemblage	3a*	3b*	3a	3b	4a	4b		
wt.%								
SiO_2	64.9	44.6	65.7	43.2	67.3	22.5	59.4	0.3
Al_2O_3	17.5	20.6	16.7	16.8	16.9	6.7	16.8	0.4
FeO	1.0	7.0	1.2	5.7	0.2	2.8	2.5	11.1
MnO	0.0	0.0	0.0	0.2	0.0	0.3	0.1	35.9
MgO	0.7	4.0	0.4	1.9	0.1	0.9	0.8	10.7
CaO	1.2	14.4	1.7	22.6	0.4	38.8	7.6	105.0
Na_2O	1.4	3.4	1.5	2.6	0.9	1.2	1.8	1.3
K_2O	13.2	1.0	12.6	0.2	14.1	0.1	9.1	0.01
CO_2	0.0	3.3	0.0	6.8	0.0	26.6	1.9	
H_2O	0.1	1.4	0.0	0.0	0.0	0.0	0.0	

The approximate composition of the initial liquid L was calculated by combining the composition of domains 3a and 3b in a 70:30 ratio. LSr and LCr compositions are derived from those of the 4a and 4b mineral assemblages.

domain. The residual liquid Lr occupied interstitial positions between the crystallising minerals. Crystallization also occurred within the melt pod isolated in Cpx1, producing different assemblages compared to those in the matrix (i.e., assemblages 3a* and 3b*).

Stage 4: liquid immiscibility and late crystallization. During this stage, immiscibility occurred between a residual carbonate liquid (LCr) and a residual silicate liquid (LSr), which were exsolved from the residual carbonated silicate melt Lr. Fine-grained Kfs + Qz ± Cpx (assemblage 4a) eventually crystallized from LSr, forming interstitial domains (i.e., silicate domain 4a) characterized by a grain size significantly finer than that of the surrounding matrix. The final crystallization of residual LCr led to the development of two distinct types of mineral associations (i.e., carbonate domains 4b): (i) fine-grained, interstitial symplectitic aggregates of Scp + Qz, and (ii) fine-grained Cal occupying interstitial positions at the grain boundaries of the medium-grained Kfs3a.

The sharp physical separation between the carbonate domains 3b (i.e., the calc-silicate ocelli) and the silicate domain 3a in both the leucosome matrix and the melt pod isolated within Cpx1, may also suggest early liquid immiscibility during stage 3, at the onset of melt crystallization. In that case, the medium-grained assemblage 3a (Kfs + Qz + Cpx; i.e., silicate domain 3a) and the granoblastic aggregates of Scp + Cpx + Cal (assemblage 3b), would represent the crystallization products of two immiscible silicate and carbonate liquids (LS–LC), which were exsolved from L during the initial cooling stage. According to this hypothesis, liquid immiscibility was possibly triggered by the back-reactions between Cpx1/Grt1 and the surrounding melt, as well as by decompression, which decreased the CO_2 solubility in the melt L[52]. This alternative interpretation is summarized in Supplementary Fig. S12.

Compositions and partition coefficients of the residual silicate and carbonate melts

The residual silicate liquid LSr is trachytic in composition (Table 1; Supplementary Fig. S13), enriched in alkalis and SiO_2 compared to the initial liquid L. Its conjugate carbonate liquid LCr is relatively high in SiO_2 (i.e., $SiO_2 \approx 22$ wt.%), and therefore its crystallization product should be formally classified as silico-carbonatite, having $SiO_2 > 20$ wt.%[66], although it actually falls within the carbonatite *sensu lato* definition of Ref. 43 (i.e., any rock containing > 30 vol.% primary igneous carbonate regardless of silica content).

To confirm the conjugate nature of the LSr-LCr pair, their major element partition coefficients D(LCr/LSr) were calculated and compared with those experimentally determined by Ref. 42. Following Ref. 42,67, the partitioning coefficients calculated for the LSr-LCr pair are reported as a function of ionic potential (i.e., the charge/ionic radius ratio, Z/r, of each element) in Fig. 6. It emerges that K_2O is strongly partitioned into the silicate liquid, with D = 0.01, while Na_2O is partitioned into the carbonate liquid, with D = 2.5. CaO has the highest partition coefficient (D = 105.0) and is therefore predominantly sequestered within the carbonate liquid. Similarly, MnO, MgO and FeO are preferentially incorporated into the carbonate liquid, with D values of 35.9, 10.7, and 11.1, respectively. Both Al_2O_3 and SiO_2 have D < 1 and are therefore partitioned into the silicate liquid (D = 0.4 for Al_2O_3; D = 0.3 for SiO_2). Overall, the calculated D values are consistent with the trend in experimentally determined partition coefficients of Ref. 42 for H_2O-bearing, silica-rich, potassic systems. Particularly well reproduced are: (i) the positive correlation between the partition coefficients of alkalis and alkaline earth elements and the ionic potential Z/r (Fig. 6), a distinctive feature of potassic systems (i.e., Na<<K), but not of sodic (Na>>K) and alkalic (Na ≈ K) systems; (ii) the very high (>>1) or very low (<<1) values of the partition coefficients for all elements, which are especially characteristics of H_2O-bearing systems (and also of SiO_2-rich systems); this led to the separate crystallization of Na_2O- and CaO- (i.e., calcite + scapolite) and K_2O- (i.e., K-feldspar) bearing phases in distinct interstitial domains of the leucosomes[67].

Compared to most carbonatitic melts produced by immiscibility experiments[42,68–73], LCr is relatively enriched in SiO_2 and depleted in alkalis (Fig. 7). However, most immiscibility experiments on compositions closer-to-natural melts[42,68–73] used SiO_2-undersaturated, alkali-enriched, starting materials that approximate variably carbonated and metasomatized peridotites, which differ significantly from the average composition of carbonate-bearing sediments[9,10] (Fig. 7a). Silicate–carbonate liquid immiscibility has been reported from a few experiments based on starting materials representative of carbonate-bearing sediments (i.e., marl and calcareous pelite[74,75]) at pressure ≥ 2.5 GPa. The carbonate liquids generated through this process are characterized by lower alkali contents compared to most experimental carbonatitic melts (Fig. 7b). This indicates a strong correlation between the composition of the silicate–carbonate melts and that of the initial melt from which the conjugate liquids are generated. The fact that the composition of LCr identified in the studied migmatitic metamarls is fully consistent with those of natural crustal-derived carbonatites[37] (Fig. 7b) further supports this hypothesis, and highlights the need for specifically designed experiments to investigate immiscibility behaviour in carbonate-bearing sediment analogue materials. Only such experimental studies would eventually elucidate whether the observed Scp + Cpx + Cal ocelli (assemblage 3b) actually represent the crystallization product of an immiscible carbonate liquid LC separated from a silicate liquid LS during the initial cooling stage, possibly reconciling the microstructural record with the experimental evidence.

Genesis of orogenic carbonatites and implications for their mobility in the crust

Since the 1960s, carbonatites have mainly been interpreted as mantle-derived magmas formed by low degrees of partial melting of carbonated peridotites (cf. review by Ref. 36,76–78). This view is supported by isotopic signatures, trace-element patterns, and associations with mantle rocks[79,80]. In a seminal paper, Mitchell (2005)[43] proposed that carbonate-rich rocks formed by anatectic melting of crustal rocks should not be classified as carbonatites. This considerably questioned an igneous origin and suggested alternative terms such as mobilised calc-silicate skarns, anatectic skarns, or anatectic calc-silicate veins

Recent petrological and geochemical data suggested the possibility of a crustal source for carbonate magmas, with several studies providing strong evidence that carbonate melts can indeed form through partial melting of crustal rocks. Su et al. (2024a)[37] recently introduced the term para-carbonatite to describe carbonate igneous rocks that crystallise from a liquid

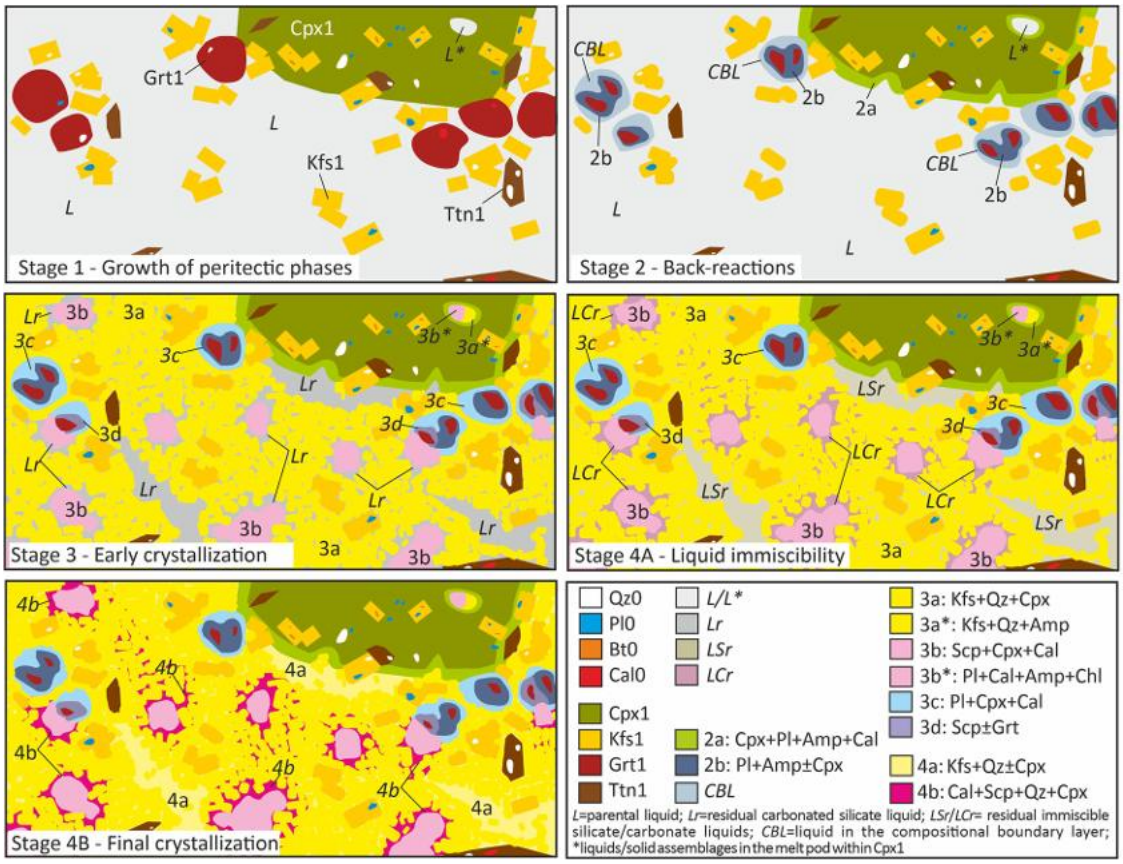

Fig. 5 | Simplified sketch summarizing the anatectic evolution inferred for the studied samples. Stage 4 is divided in two sub-stages (Stage 4a: liquid immiscibility; Stage 4b: late crystallization). Note that assemblage 2a refers to the spongy clinopyroxene 2a and its inclusions of plagioclase, amphibole and calcite, while assemblage 2b refers to the kelyphitic corona around garnet, consisting of amphibole, plagioclase, ± clinopyroxene.

generated by the partial melting of carbonate-bearing (meta)sedimentary rocks within the Earth's crust, distinguishing them from ortho-carbonatite, which refers to igneous rocks mostly composed of carbonates that crystallise from mantle-derived melts[43,66]. Yaxley et al. (2022)[36] used the term anatectic carbonatites to describe the same type of rocks, noting that recognising these rocks can be challenging, especially when melt migration is limited, which prevents anatectic carbonatite melts from escaping their (meta)sedimentary source rocks. Although the occurrences of anatectic carbonatites have been increasingly recognised in recent years[37], their genesis remains unclear.

Our findings provide direct evidence of (silico-)carbonatitic melts formed through in situ partial melting of mixed silicate–carbonate metasediments within an orogenic setting, a process not previously documented in natural systems. The textural association of fine-grained silicate vs calc-silicate assemblages (K-feldspar vs calcite ± scapolite) interstitially crystallized in distinct domains of the leucosome supports liquid immiscibility as a plausible mechanism for producing carbonate melts. From a microstructural point of view, the calc-silicate ocelli embedded in the silicate matrix might also be interpreted as crystallized droplets of (silico-)carbonate melt exsolved from a carbonated silicate liquid during the early cooling stage. Indeed, similar immiscibility microstructures have been observed between carbonate and silicate melts experimentally obtained for H_2O-bearing systems under comparable pressure-temperature conditions, although from different starting bulk compositions[42,81,82]. In such experiments, near-perfect phase separation is evidenced by quenched carbonate melt droplets or globules within a silicate melt glass matrix, or vice versa. In natural systems, microstructural evidence of immiscibility between carbonate and silicate melts has been mainly reported from melt inclusions[27,79,83–85] where rounded carbonate droplets embedded in a silicate matrix and sharp phase boundaries between the two phases indicate separation of immiscible melts. Whatever the interpretation (i.e., liquid immiscibility occurred during the earlier or later cooling stages), the final conclusion remains unchanged: partial melting of meta-marls can generate carbonate-rich melts. This crustal model offers a new perspective on the genesis of carbonatites, expanding the petrogenetic framework to include anatexis of carbonate-bearing sediments in orogenic crust. It emphasizes that carbonatitic melts can form in the absence of mantle-derived magmatism, without needing ultramafic precursors or partial melting deep in the mantle. Instead, regional (or contact) metamorphism and the presence of carbonate-rich sedimentary protoliths provide conditions sufficient for generating carbonatitic melts. Furthermore, if a marly protolith is involved, alkalis and H_2O are internally available in the system, potentially lowering the *solidus* to temperatures compatible with the amphibolite-to-granulite-facies transition, without the need for externally-derived aqueous fluids fluxing as proposed by Ref. 19 for nearly pure carbonatic systems. These findings align with recent experimental[17,19] and field-based studies[37], including melt inclusions from high-grade metamorphic terranes, which document carbonate-rich liquids of non-mantle origin[27].

Recognising crustal anatexis as a viable pathway for forming carbonatites requires a re-evaluation of genetic models for carbonatites in collisional and metamorphic environments. In such geological settings, when mantle-derived signals are unclear or absent (e.g., the C–O isotopic signature is clearly distinct from that of mantle-derived carbonatites[32,34]), a supracrustal origin should be considered. Our data, along with previous reports[37], suggest that crustal carbonatites are not merely local anomalies but rather an essential and previously underestimated aspect of carbon mobility and magmatism within the continental lithosphere.

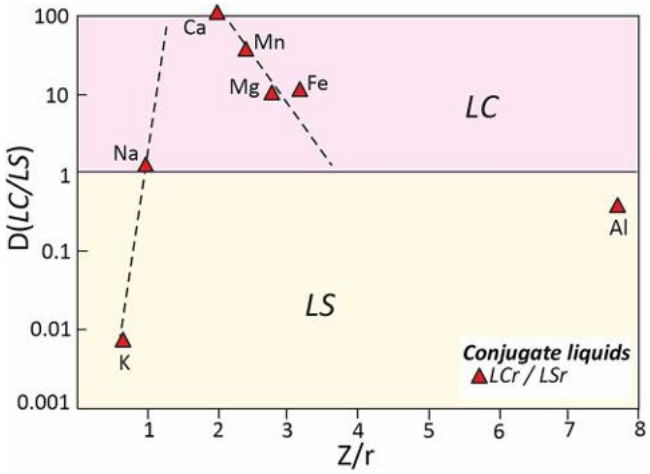

Fig. 6 | Partition coefficients of conjugate carbonate and silicate residual melts. Partition coefficients D(LC/LS) for major element oxides between conjugate carbonate and silicate residual liquids (LCr and LSr), plotted as a function of the ionic potential (charge/ionic radius; radii from Ref. 95). The dashed lines represent trend lines for given cation groups[42]. Na, Ca, Mn, Mg and Fe partition into the carbonate melt, while K, Al (and Si) in the silicate liquid. The estimated partition coefficients are consistent with those experimentally determined by Ref. 42 for H_2O-bearing silica-rich potassic systems.

This finding adds to the ongoing debate about the mobility of carbonate melts within crustal environments. Carbonatite magmas are well known for their high mobility, due to their very low viscosities (0.01–0.1 Pa·s), densities, low dihedral angles (< 60°) at grain boundaries, and high volatile contents[80,86]. These properties suggest that carbonate melts can be inherently highly mobile. However, when a viscous silicate melt is present, the carbonate melt phase may remain arrested due to disrupted melt connectivity until the silicate component begins crystallising[86]. This interaction delays migration even if immiscibility promotes early segregation. Field observations of carbonate melt mobility in crustal settings, such as in Ref. 23, confirm that when structural pathways and rheological conditions are favourable, carbonate melts can indeed migrate through the crust. In the contact aureole of the Adamello intrusion (Italy), these authors[23] documented carbonate melts forming along grain boundaries, triple junctions, and pressure shadows, demonstrating effective melt segregation and channelization. These structures provided low-viscosity pathways, enhancing melt extraction. The rheological weakening of the host rock due to melt infiltration further enhanced transport by reducing the strength of the solid matrix. Their study also showed that the presence of early-formed silicate minerals (e.g., clinopyroxene and K-feldspar) helped frame a rigid scaffold that enabled carbonate melts to percolate through a partially molten yet structurally coherent system. This combination of mechanically coherent frameworks and localized permeability zones is crucial for allowing carbonate melt migration at crustal depths.

Our data challenge the general view that Earth's carbon mobility is mainly governed by mantle processes and highlight the possibility that crustal melting of carbonate-bearing rocks can play a role in the long-term carbon cycling. More broadly, recognizing that anatectic melting of carbonate-bearing sediments can generate carbonatitic melts fundamentally revises our understanding of the crustal carbon cycle. Anatectic carbonate melts imply that the continental crust is not simply a degassing or passive degassing zone for deep carbon fluids and melts, but an active carbon source, especially under thickened crust and high geothermal gradients. Depending on whether these melts crystallize in situ or migrate upwards, the crust may act as a transient CO_2 reservoir or impact orogenic carbon fluxes. These findings emphasize the importance of including crustal carbonatite formation into future models of Earth carbon cycling and tectonic degassing.

Methods

Sample location

The studied sample was collected from the upper structural levels of the Greater Himalayan Sequence (GHS), in eastern Nepal Himalaya. The GHS, exposed in the metamorphic core of the Himalayan belt (Supplementary Fig. S1a, b), mostly consists of a Neoproterozoic–Ordovician sedimentary sequence originally deposited on the northern edge of the Indian passive margin, and later involved in the India–Asia continental collision, which culminated in the formation of the Himalayan orogen[87]. The GHS metasedimentary sequence comprises different lithologies derived from protoliths ranging from pure pelites to calcareous pelites, with minor intercalations of marls and impure limestones[9,88]. In the upper half of the GHS, abundant augen gneisses and bodies of two-micas and tourmaline-bearing leucogranites are also present. The GHS experienced a Barrovian-type metamorphism, with increasing peak temperature conditions toward structurally higher levels[41,87]; a progressive decrease of maximum pressure is instead observed upward, as testified by the transition from garnet + K-feldspar + sillimanite ± kyanite assemblages to K-feldspar + sillimanite + cordierite ± garnet assemblages[41,89,90].

The studied samples were collected from the Upper-GHS exposed in the Ilam region of far eastern Nepal (sample 19a-50: N27°01'16.7", E87°41'53.3"; 2040 m a.s.l.; Supplementary Fig. S1b, c). In that region, garnet + K-feldspar + sillimanite + biotite anatectic gneisses are mostly exposed, with abundant intercalations of calc-silicate gneisses (Supplementary Fig. S1d). The occurrence of radial aggregates of prismatic sillimanite in equilibrium with peritectic K-feldspar in the garnet + tourmaline-bearing granitic leucosomes and pods (e.g., sample 19a-51b; N27°01'01.0", E87°41'53.1", 2050 m a.s.l.; Supplementary Fig. S1e) allows constraining peak metamorphic conditions of about 750–800 °C, 0.7–0.8 GPa for this portion of the GHS[41], i.e., biotite dehydration melting occurred in the sillimanite stability field.

Optical microscopy and CL imaging

Petrographic observations were made on three thin sections (19a-50_1; 19a-50_2; 19a-50_3) obtained from the same sample, using an Olympus BX41 transmitted-light microscope at the Department of Earth Sciences, University of Torino, Italy. Large-area image mosaics of the whole thin sections were acquired at the same microscope, equipped with a digital camera DP23-CU and the software PRECiV Core, Version 2.1, using the 1.25 objective with plane polarized (PPL) and crossed polarized (XPL) light. The mosaics were manually assembled using CorelDraw 2020.

Optical cathodoluminescence (CL) was used to further investigate the microstructural features of the samples at the thin section scale. CL images were acquired using a CITL 8200 mk3 cathodoluminescence microscope stage operating at 15–17 kV and a current of 400–500 mA, installed at the Department of Earth Sciences, University of Torino, Italy.

SEM-EDS analyses and maps

High-resolution multispectral mapping was performed on the entire thin sections (ca. 3 cm × 1.5 cm) to highlight their microstructures at the thin-section scale. These X-ray maps were obtained using a JEOL IT300LV Scanning Electron Microscope (SEM) hosted at the Department of Earth Sciences, University of Torino, Italy. The instrument is equipped with an Oxford Aztec energy-dispersive spectrometry (EDS) and an Oxford ULTIMAX65 silicon drift detector. For this kind of detector, the Aztec Live software (Oxford Instruments) was used. The operating conditions used for large mapping are: 15 kV acceleration voltage, process time 3, 3 frame counts, 2048 × 1536 pixel resolution (ca. 1.5 µm spot distance), and 20 ms pixel dwell time (ca. 1 min frame live time). High-resolution multispectral mapping was additionally performed on nine smaller areas to highlight specific microstructural details; these small maps were obtained using the same instrument but different operating conditions: 15 kV acceleration voltage, process time 3, 3 frame counts, 4096 × 3072 pixel resolution (ca. 0.5 µm spot distance), and 60 ms pixel dwell time (ca. 13 min frame live time).

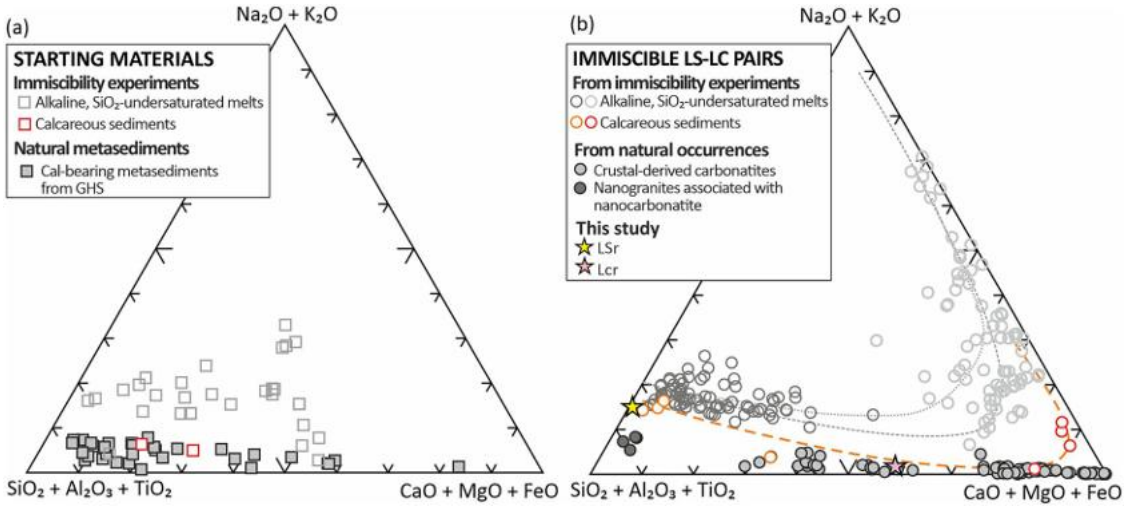

Fig. 7 | Hamilton projections[96] comparing compositions of starting materials and melting products from experimental and natural data. a Starting materials include those related to immiscibility experiments[42,68–75] and the calcite-bearing metasediments from the Greater Himalayan Sequence (i.e., the source-rocks of the studied migmatitic meta-marls)[9,10]. **b** Melting products include the silicate–carbonate liquid pairs generated by the same immiscibility experiments as in (**a**) and the natural crustal-derived carbonatites[37]. Composition of nanogranites coexisting with nanocarbonatites analysed by Ref. 27 are also reported in (**b**) (note that the composition of nanocarbonatites was not analysed in that study). The approximate compositions of LSr and LCr derived in this study are plotted in (**b**): they are fully consistent with the natural record of crustal-derived carbonatites and with the few experimental data for calcareous sediments[74,75]. Experimental data are plotted independently of the pressure and temperature at which they have been obtained. Grey and orange dashed or dotted curves in (**b**) delineate the miscibility gap between silicate and carbonate liquids as reported by Ref. 78 for MgO in the silicate melt, respectively ≤ 3.8 wt.% (grey dashed line) and > 3.8 wt.% (grey dotted), and by Ref. 75 (orange dashed).

The rock-forming minerals were analysed with the same SEM-EDS instrument used for the high-resolution X-ray maps. The operating conditions for spot analyses are: 15 kV accelerating voltage, a 10 mm working distance, a process time 3, HighProbe current mode, and a 15 s counting time. Quantitative SEM-EDS data were acquired and processed using the software Aztec Live 6.1 (Oxford Energy). Natural oxides and silicates standards from Astimex Scientific Limited were used to calibrate the raw data; the ΦρZ correction was applied. Most analyses were recalculated and plotted using MinPlotX[91]; amphibole group minerals were normalised according to Ref. 92, while for carbonates the NORM computer program[93] was used. XMg for clinopyroxene is defined as XMg=Mg/(Mg+Fe^{2+}), XAn and XAb for feldspars are defined as XAn=Ca/(Ca+Na+K), XAb=Na/(Ca+Na+K) and XMe for scapolite is defined as XMe = ΣMe^{2+}, where Me^{2+} are divalent metal cations.

Bulk compositions of residual silicate and carbonate conjugate liquids and of the initial liquid L

Raw data for both large and small X-ray maps were processed using MultiSpec© software (Purdue Research Foundation, USA) to obtain the modal compositions of the silicate and carbonate domains (i.e., silicate domains: 3a*, 3a, 4a; carbonate domains: 3b*, 3b, 4b; Fig. 3a, b). The bulk composition of each domain was calculated by combining mineral modes and compositions and considering the molar volumes of each phase. The mineral modes and compositions used are reported in Supplementary Data S2. The bulk compositions of the silicate (4a) and carbonate (4b) domains were used as a proxy of the composition of the liquids from which they crystallized, i.e., the compositions of the residual conjugate LSr-LCr pair were approximated to those of domains 3b and 4b in the matrix. An approximate composition of the whole leucosome pod was calculated by combining the compositions of domains 3a and 3b in a 70:30 ratio, according to the observed proportions of these domains in the studied samples (see Fig. 3a, b); this composition approximates that of the initial liquid L. This approach was based on the assumption that the major-element compositions of the different (solid) domains reflect those of melts from which they derive; this assumption is supported by the absence of evidence for either significant melt extraction from the system or interactions between the melt and the host rock. However, it is to be noted that H_2O was lost during cooling and crystallization (see discussion in the text); therefore, its original amount in the various liquid generations is unknown. The degree of polymerization of the parental liquid L is expressed in terms of NBO/T ratio as defined by Ref. 94, with NBO = non-bridging oxygens associated with the presence of network modifier cations (i.e., Ca^{2+}, Mg^{2+}, Fe^{2+}, Na^{+}, K^{+}), and T = network-forming cations (i.e., Si^{4+}, Al^{3+}). #K is the molar ratio $K_2O/(K_2O + Na_2O)$.

Data availability

Most data generated or analyzed during this study are included in this published article (and its Supplementary Information file). The whole set of mineral chemical data discussed in the text (Supplementary Data S1), the spreadsheets used to reconstruct the bulk compositions of each compositional domain (Supplementary Data S2) and the source data used for Fig. 7 (Supplementary Data S3) are available in the Zenodo repository at: 10.5281/zenodo.19345712.

Received: 30 July 2025; Accepted: 21 April 2026;
Published online: 05 May 2026

References

1. Le Breton, N. L. & Thompson, A. B. Fluid-absent (dehydration) melting of biotite in metapelites in the early stages of crustal anatexis. *Contrib. Mineral. Petrol.* **99**, 226–237 (1988).
2. Vielzeuf, D. & Holloway, J. R. Experimental determination of the fluid-absent melting relations in the pelitic system. *Contrib. Mineral. Petrol.* **98**, 257–276 (1988).
3. Patiño Douce, A. E. & Johnston, A. D. Phase equilibria and melt productivity in the pelitic system: implications for the origin of peraluminous granitoids and aluminous granulites. *Contrib. Mineral. Petrol.* **107**, 202–218 (1991).
4. Patiño Douce, A. E. & Beard, J. S. Dehydration-melting of biotite gneiss and quartz amphibolite from 3 to 15 kbar. *J. Petrol.* **36**, 707–738 (1995).
5. Gardien, V., Thompson, A. B., Grujic, D. & Ulmer, P. Experimental melting of biotite + plagioclase + quartz ± muscovite assemblages

and implications for crustal melting. *J. Geophys. Res.* **100**, 15581–15591 (1995).
6. Stevens, G., Clemens, J. D. & Droop, G. T. Melt production during granulite-facies anatexis: experimental data from "primitive" metasedimentary protoliths. *Contrib. Mineral. Petrol.* **128**, 352–370 (1997).
7. Brown, M. Granite: from genesis to emplacement. *GSA Bull.* **125**, 1079–1113 (2013).
8. Johnson, T., Yakymchuk, C. & Brown, M. Crustal melting and suprasolidus phase equilibria: From first principles to the state-of-the-art. *Earth-Sci. Rev.* **221**, 103778 (2019).
9. Groppo, C., Rapa, G., Frezzotti, M. L. & Rolfo, F. The fate of calcareous pelites in collisional orogens. *J. Metam. Geol.* **39**, 181–207 (2021).
10. Tamang, S., Groppo, C., Girault, F., Perrier, F. & Rolfo, F. Metamorphism of Dolomitic And Magnesitic Rocks In Collisional Orogens And Implications For Orogenic CO_2 Degassing. *J. Petrol.* **65**, egae021 (2024).
11. Wyllie, P. J. & Tuttle, O. F. Melting of calcite in the presence of water. *Am. Mineral.* **44**, 453–459 (1959).
12. Wyllie, P. J. & Tuttle, O. F. The System CaO-CO_2-H_2O and the origin of carbonatites. *J. Petrol.* **1**, 1–46 (1960).
13. Cooper, A. F., Gittins, J. & Tuttle, O. F. The system Na_2CO_3-K_2CO_3-$CaCO_3$ at 1 kilobar and its significance in carbonatite petrogenesis. *Am. J. Sci.* **275**, 534–560 (1975).
14. Boettcher, A. L., Robertson, J. K. & Wyllie, P. J. Studies in synthetic carbonatite systems: solidus relationships for CaO-MgO-CO_2-H_2O to 40 kbar and CaO-MgO-SiO_2-CO_2-H_2O to 10 kbar. *J. Geophys. Res.* **85**, 6937–6943 (1980).
15. Otto, J. W. & Wyllie, P. J. Relationships between silicate melts and carbonate-precipitating melts in CaO-MgO-SiO_2-CO_2-H_2O at 2 kbar. *Mineral. Petrol.* **48**, 343–365 (1993).
16. Lee, W. J., Huang, W. L. & Wyllie, P. Melts in the mantle modeled in the system CaO-MgO-SiO_2-CO_2 at 2.7 GPa. *Contrib. Mineral. Petrol.* **138**, 199–213 (2000).
17. Durand, C., Baumgartner, L. P. & Marquer, D. Low melting temperature for calcite at 1000 bars on the join $CaCO_3$-H_2O. Some geological implications. *Terra Nova* **27**, 364–369 (2015).
18. Weidendorfer, D., Manning, C. E. & Schmidt, M. W. Carbonate melts in the hydrous upper mantle. *Contrib. Mineral. Petrol.* **175**, 72 (2020).
19. Liu, P., Massonne, H. J., Wei, C., Lu, Y. & Lu W. Melting relationships of calcite-dolomite-H_2O at 1 GPa and implications for partial melting of metacarbonate rocks in deeply buried crust. *J. Petrol*. egaf061 (2025).
20. Lentz, D. R. Carbonatite genesis: a reexamination of the role of intrusion-related pneumatolytic skarn processes in limestone melting. *Geology* **27**, 335–338 (1999).
21. Ganino, C., Arndt, N. T., Chauvel, C., Jean, A. & Athurion, C. Melting of carbonate wall rocks and formation of the heterogeneous aureole of the Panzhihua Intrusion. *China Geosci. Front.* **4**, 535–546 (2013).
22. Wenzel, T., Baumgartner, L. P., Brügmann, G. E., Konnikiv, E. G. & Kislov, E. V. Partial melting and assimilation of dolomitic xenoliths by mafic magma: the Ioko-Dovyren intrusion (north Baikal Region, Russia). *J. Petrol.* **43**, 2049–2074 (2002).
23. Floess, D., Baumgartner, L. P. & Vonlanthen, P. An observational and thermo- dynamic investigation of carbonate partial melting. *Earth Planet. Sci. Lett.* **409**, 147–156 (2015).
24. Xu, X. et al. Melt inclusion evidence for limestone assimilation, calc-silicate melts, and "magmatic skarn. *Geology* **51**, 5 (2023).
25. Liu, Y., Berner, Z., Massonne, H. J. & Zhong, D. Carbonatite-like dykes from the eastern Himalayan syntaxis: geochemical, isotopic, and petrogenetic evidence for melting of metasedimentary carbonate rocks within the orogenic crust. *J. Asian Earth Sci.* **26**, 105–120 (2006).
26. Morteani, G., Kostitsyn, Y. A., Gilg, H. A., Preinfalk, C. & Razakamanana, T. Geochemistry of phlogopite, diopside, calcite, anhydrite and apatite pegmatites and syenites of southern Madagascar: evidence for crustal silicocarbonatitic (CSC) melt formation in a Panafrican collisional tectonic setting. *Int. J. Earth Sci.* **102**, 627–645 (2013).
27. Ferrero, S., Wunder, B., Ziemann, M. A., Wälle, M. & O'Brien, P. J. Carbonatitic and granitic melts produced under conditions of primary immiscibility during anatexis in the lower crust. *Earth Planet. Sci. Lett.* **454**, 121–131 (2016).
28. Schumann, D., Martin, R. F., Fuchs, S. & De Fourestier, J. Silicocarbonatitic melt inclusions in fluorapatite from the Yates prospect, Otter Lake, Québec: evidence of marble anatexis in the central metasedimentary belt of the Grenville Province. *Can. Mineral.* **57**, 583–604 (2019).
29. Hegner, E. et al. Sediment-Derived Origin of the Putative Munnar Carbonatite, South India. *J. Asian Earth Sci.* **200**, 104432 (2020).
30. Wang, J. et al. Crustal derivation of the ca. 475 Ma Eppawala carbonatites in Sri Lanka. *J. Petrol.* **62**, egab075 (2021).
31. Martin, R. F., Schumann, D. & Dharmapriya, P. L. Dolomitic marble in a context of UHT metamorphism: possible signs of melting, Lenadora Quarry, Sri Lanka. *J. Petrol.* **63**, 1–15 (2022).
32. Wu, H., Zhu, W. & Ge, R. Evidence for carbonatite derived from the Earth's crust: The late Paleoproterozoic carbonate-rich magmatic rocks in the Southeast Tarim Craton, Northwest China. *Precamb. Res.* **369**, 106425 (2022).
33. Wang, C., Foley, S. F., Liu, Y., Wang, Y. & Xu, Y. G. Origin of carbonate melts in orogenic belts by anatexis of downthrust carbonate sediments. *Earth Planet. Sci. Lett.* **619**, 18303 (2023).
34. Su, B. X. et al. Crustal anatectic origin of the pegmatitic carbonate rocks in the Proterozoic Highland Complex, Sri Lanka. *Contrib. Mineral. Petrol.* **179**, 96 (2024).
35. Wickramasinghe, W. A. G. K. et al. An unusual occurrence of carbonatites derived from the crust in the UHT Granulite Facies metamorphic terrain of Sri Lanka. *Precamb. Res.* **450**, 107502 (2024).
36. Yaxley, G. M., Anenburg, M., Tappe, S., Decree, S. & Guzmics, T. Carbonatites: classification, sources, evolution, and emplacement. *Annu. Rev. Earth Planet. Sci.* **50**, 261–293 (2022).
37. Su, B.-X., Wang, S.-Y., Wang, J. & Fan, H.-R. Crustal-derived versus mantle-derived carbonatites. *Lithos* **488–489**, 107826 (2024).
38. Sawyer, E. W. Criteria for the recognition of partial melting. *Phys. Chem. Earth Solid Earth Geod.* **24**, 269–279 (1999).
39. Maroni, A. et al. Similar microstructures, different interpretations: the possible anatectic record of granulite-facies marbles. *J. Petrol.* egag033 (2026),
40. Özkan, M., Çelik, O. F., Marzoli, A., Çörtük, R. M. & Billor, M. Z. The origin of carbonatites from the eastern Armutlu Peninsula (NW Turkey). *J. Geol. Soc.* **178**, jgs2020–2171 (2021).
41. Rolfo, F., Groppo, C. & Mosca, P. Petrological constraints of the "Channel Flow" model in eastern Nepal. In: Mukherjee, S., Carosi, R., van der Beek, P.A., Mukherjee, B.K. & Robinson, D.M. (eds), "Tectonics of the Himalaya". Geol. Soc. of London, SP, **412**, 177–197 (2015).
42. Martin, L. H. J., Schmidt, M. W., Mattisson, H. B. & Guenther, D. Element partitioning between immiscible carbonatite and silicate melts for dry and H_2O-bearing Systems at 1-3 GPa. *J. Petrol.* **54**, 2301–2338 (2013).
43. Mitchell, R. H. Carbonatites and carbonatites and carbonatites. *Can. Mineral.* **43**, 2049–2068 (2005).
44. Warr, L. N. IMA–CNMNC approved mineral symbols. *Mineral. Mag.* **85**, 291–320 (2021).
45. Sawyer, E. W. Melt segregation in the continental crust: distribution and movement of melt in anatectic rocks. *J. Metamorph. Geol.* **19**, 291–309 (2001).
46. Holness, M. B. & Sawyer, E. W. On the pseudomorphing of melt-filled pores during the crystallization of migmatites. *J. Petrol.* **49**, 1343–1363 (2008).
47. Brown, M. The mechanism of melt extraction from lower continental crust of orogens. *Spec. Pap. Geol. Soc. Am.* **389**, 35–48 (2004).

48. White, R., Powell, R. & Halpin, J. Spatially-focussed melt formation in aluminous metapelites from Broken Hill, Australia. *J. metamorph. Geol.* **22**, 825–845 (2004).
49. Taylor, J. & Stevens, G. Selective entrainment of peritectic garnet into S-type granitic magmas: evidence from Archaean mid-crustal anatectites. *Lithos* **120**, 277–292 (2010).
50. Festa, V., Spiess, R. & Tursi, F. Garnet coalescence clogs melt extraction channels in migmatite. *Lithos* **472–473**, 107581 (2024).
51. Stüwe, K. & Powell, R. Metamorphic segregations associated with garnet and othopyroxene porphyroblast growth: two examples from the Larsemann Hills, east Antarctica. *Contrib. Mineral. Petrol.* **103**, 523–530 (1989).
52. Duncan, M. S. & Dasgupta, R. CO_2 solubility and speciation in rhyolitic sediment partial melts at 1.5–3.0 GPa–implications for carbon flux in subduction zones. *Geochim. Cosmochim. Acta* **124**, 328–347 (2014).
53. Carvalho, B. B., Bartoli, O. & Cesare, B. C–O–H fluid-melt-rock interaction in graphitic granulites and problems of quantifying carbon budget in the lower continental crust. *Chem. Geol.* **631**, 121503 (2023).
54. Tamic, N., Behrens, H. & Holtz, F. The solubility of H_2O and CO_2 in rhyolitic melts in equilibrium with a mixed CO_2–H_2O fluid phase. *Chem. Geol.* **174**, 333–347 (2001).
55. Brooker, R. A., Kohn, S. C., Holloway, J. R. & McMillan, P. F. Structural controls on the solubility of CO_2 in silicate melts. Part I: bulk solubility data. *Chem. Geol.* **174**, 225–239 (2001).
56. Beherens, H. et al. Solubility of H_2O and CO_2 in ultrapotassic melts at 1200 and 1250 °C and pressure from 50 to 500 MPa. *Am. Mineral.* **94**, 105–120 (2009).
57. Morizet, Y., Paris, M., Gaillard, F. & Scaillet, B. Carbon dioxide in silica-undersaturated melt. Part I: The effect of mixed alkalis (K and Na) on CO_2 solubility and speciation. *Geoch. Cosmoch. Acta* **141**, 45–61 (2014).
58. Zellmer, G. F. et al. Inferring the effects of compositional boundary layers on crystal nucleation, growth textures, and mineral chemistry in natural volcanic tephras through submicron-resolution imaging. *Front. Earth Sci.* **4**, 88 (2016).
59. Honour, V. C. et al. Compositional boundary layers trigger liquid unmixing in a basaltic crystal mush. *Nat. Comm.* **10**, 4821 (2019).
60. Wang, W. et al. Formation of spongy clinopyroxene: Insights from eclogitic inclusions in diamonds. *J. Petrol.* **66**, egaf036 (2025).
61. Carpenter, R. L., Edgar, A. D. & Thibault, Y. Origin of spongy textures in clinopyroxene and spinel from mantle xenoliths, Hessian Depression, Germany. *Mineral. Petrol.* **74**, 149–162 (2002).
62. Bonadiman, C., Coltorti, M., Beccaluva, L. & Siena, F. Kimberlite-like metasomatism and 'Garnet Signature' in Spinel-peridotite Xenoliths from Sal, Cape Verde Archipelago: Relics of a Subcontinental Mantle Domain within the Atlantic Oceanic Lithosphere? *J. Petrol.* **46**, 2465–2493 (2005).
63. Shaw, C. S. J., Heidelbach, F. & Dingwell, D. B. The origin of reaction textures in mantle peridotite xenoliths from Sal Island, Cape Verde: the case for "metasomatism" by the host lava. *Contrib. Mineral. Petrol.* **151**, 681–697 (2006).
64. Ezad, I. S. et al. Kelyphite textures experimentally reproduced through garnet breakdown in the presence of a melt phase. *J. Petrol.* **63**, 1–22 (2022).
65. Guo, S. et al. Formation of carbon-bearing silicate melts by melt-metacarbonate interaction at convergent plate margins. *Earth Planet. Sci. Lett.* **597**, 117816 (2022).
66. Le Maitre, R. W. Igneous Rocks: A Classification and Glossary of Terms. Cambridge Univ. Press, Cambridge, UK (2002).
67. Veksler, I. V. Liquid immiscibility and its role at the magmatic-hydrothermal transition: a summary of experimental studies. *Chem. Geol.* **210**, 7–31 (2004).
68. Freestone, I. C. & Hamilton, D. L. The role of liquid immiscibility in the genesis of carbonatites-an experimental study. *Contrib. Mineral. Petrol.* **73**, 105–117 (1980).
69. Kjarsgaard, B. A., Hamilton, D. L. & Peterson, T. D. Peralkaline nephelinite/carbonatite liquid immiscibility: comparison of phase compositions in experiments and natural lavas from Oldoinyo Lengai. In: Bell, K. & Keller, J. (eds) Carbonatite volcanism, Oldoinyo Lengai and the petrogenesis of natrocarbonatites. Berlin: Springer, pp.163–190 (1995).
70. Kjarsgaard, B. A. Phase relations of a carbonated high-CaO nephelinite at 0.2 and 0.5 GPa. *J. Petrol.* **39**, 2061–2075 (1998).
71. Martin, L. H. J. et al. Element partition in between immiscible carbonatite-kamafugite melts with application to the Italian ultrapotassic suite. *Chem. Geol.* **320-321**, 96–112 (2012).
72. Nabyl, Z. et al. A window in the course of alkaline magma conducive to immiscible REE-rich carbonatites. *Geochim. Cosmoch. Acta* **282**, 297–323 (2020).
73. Weidendorfer, D. & Asimov, P. D. Experimental constraints on truly conjugate alkaline silicate–carbonatite pairs. *Earth Planet. Sci. Lett.* **584**, 117500 (2022).
74. Skora, S. et al. Hydrous phase relations and trace element partitioning behaviour in calcareous sediments at subduction-zone conditions. *J. Petrol.* **56**, 953–980 (2015).
75. Thomsen, T. B. & Schmidt, M. W. Melting of carbonated pelites at 2 5–5 0 GPa, silicate–carbonatite liquid immiscibility, and potassium–carbon metasomatism of the mantle. *Earth Planet. Sci. Lett.* **267**, 17–31 (2008).
76. Yaxley, G. M., Kjarsgaard, B. A. & Jaques, A. L. Evolution of carbonatite magmas in the upper mantle and crust. *Elements* **17**, 315–320 (2021).
77. Gittins, J. & Mitchell, R. H. The genesis of calcite and dolomite carbonatitite- forming magma by liquid immiscibility: a critical appraisal. *Geol. Mag.* **160**, 1463–1480 (2023).
78. Schmidt, M. W., Giuliani, A. & Poli, S. The origin of carbonatites. Combining the rock record with available experimental constraints. *J. Petrol.* **65**, egae105 (2024).
79. Frezzotti, M. L., Touret, J. L. R. & Neumann, E. R. Ephemeral carbonate melts in the upper mantle: carbonate-silicate immiscibility in microveins and inclusions within spinel peridotite xenoliths, La Gomera, Canary Islands. *Eur. J. Mineral.* **14**, 891–904 (2002).
80. Jones, A. P., Genge, M. & Carmody, L. Carbonate melts and carbonatites. *Rev. Mineral. Geochem.* **75**, 289–322 (2013).
81. Brooker, R. A. & Kjarsgaard, B. A. Silicate-carbonatite liquid immiscibility and phase relations in the system SiO_2-Na_2O-Al_2O_3-CaO-CO_2 at 0.1–2.5 GPa with applications to carbonatite genesis. *J. Petrol.* **52**, 1281–1305 (2011).
82. Moore, K. R., Brady, A. E. & Costanzo, A. Crystal-liquid segregation of silicocarbonatite magma leads to the formation of calcite carbonatite. *J. Petrol.* **63**, 1–14 (2022).
83. Berndt, J. & Klemme, S. Origin of carbonatites — liquid immiscibility caught in the act. *Nat. Comm.* **13**, 2892 (2022).
84. Berndt, J. & Klemme, S. Reply to: Silica is unlikely to be soluble in upper crustal carbonatite melts. *Nat. Comm.* **14**, 943 (2023).
85. Guzmic, T. et al. Liquid immiscibility between silicate, carbonate and sulfide melts in melt inclusions hosted in co-precipitated minerals from Kerimasi volcano (Tanzania): evolution of carbonated nephelinitic magma. *Contrib. Mineral. Petrol.* **164**, 101–122 (2012).
86. Minarik, W. G Complications to carbonatite melt mobility due the presence of an immiscible silicate melt. *J. Petrol.* **39**, 1965–1973 (1998).
87. Kohn, M. J. Himalayan metamorphism and its tectonic implications. *Annu. Rev. Earth Planet. Sci.* **42**, 381–419 (2014).
88. Upreti, B. N. An overview of the stratigraphy and tectonics of the Nepal Himalaya. *J. Asian Earth Sci.* **17**, 577–606 (1999).
89. Groppo, C., Rolfo, F. & Mosca, P. The cordierite-bearing anatectic rocks of the Higher Himalayan Crystallines (eastern Nepal): low-pressure anatexis, melt-productivity, melt loss and the preservation of cordierite. *J. Metam. Geol.* **31**, 187–204 (2013).
90. Goscombe, B., Gray, D. & Foster, D. A. Metamorphic response to collision in the Central Himalayan Orogen. *Gondw. Res.* **57**, 191–265 (2018).

91. Walters, J. B. & Gies, N. B. MinPlotX: A powerful tool for formula recalculation, visualization, and comparison of large mineral compositional datasets. *Mineralogia* **56**, 13–22 (2025).
92. Hawthorne, F. C. et al. Nomenclature of the Amphibole Supergroup. *Am. Mineral.* **97**, 2031–2048 (2012).
93. Ulmer, P. NORM. Program for Cation and Oxygen Mineral Norms. Computer Library IKP-ETH, Zürich (1986).
94. Mysen, B. O. Structure and properties of silicate melts. Developments in Geochemistry, vol. 4. Elsevier, Amsterdam, 354 pp. (1988).
95. Shannon, R. D. Revised effective ionic-radii and systematic studies of interatomic distances in halides and chalcogenides. *Acta Crystall. SA32 (SEP1)*, 751–767 (1976).
96. Hamilton, D. L., Freestone, I. C., Dawson, J. B. & Donaldson, C. H. Origin of carbonatites by liquid immiscibility. *Nature* **279**, 52–54 (1979).

Acknowledgements

Fieldwork and laboratory work were funded by the Italian Ministry of University and Research (PRIN2017, Project No. 2017LMNLAW and PRIN2022, Project No. 2022HA8XCS). No permissions were required for sampling.

Author contributions

C.G. and F.R. conceived the project; M.L.F. and F.T. participated in the conception of the study. C.G., F.T., A.M. and S.N. acquired the data. All co-authors contributed to the discussion and to the writing of the manuscript.

Competing interests

The authors declare no competing interests.

Additional information

Supplementary information The online version contains supplementary material available at https://doi.org/10.1038/s43247-026-03572-2.

Correspondence and requests for materials should be addressed to Chiara Groppo or Maria Luce Frezzotti.

Peer review information *Communications Earth and Environment* thanks Chris Yakymchuk, Fernanda Gervasoni, Penglei Liu and the other anonymous reviewer(s) for their contribution to the peer review of this work. Primary Handling Editors: Santiago Tassara and Joe Aslin. A peer review file is available.